Delft University of Technology

Coating layer on samples with roughness
numerical study for coherent Fourier scatterometry

Kolenov, D.; Pereira, S. F.

DOI
10.1117/12.2673768

Publication date
2023

Document Version
Final published version

Published in
Modeling Aspects in Optical Metrology IX

Citation (APA)
Kolenov, D., & Pereira, S. F. (2023). Coating layer on samples with roughness: numerical study for coherent Fourier scatterometry. In B. Bodermann, & K. Frenner (Eds.), *Modeling Aspects in Optical Metrology IX* Article 126190V (Proceedings of SPIE - The International Society for Optical Engineering; Vol. 12619). SPIE. https://doi.org/10.1117/12.2673768

Important note
To cite this publication, please use the final published version (if applicable).
Please check the document version above.

Copyright
Other than for strictly personal use, it is not permitted to download, forward or distribute the text or part of it, without the consent of the author(s) and/or copyright holder(s), unless the work is under an open content license such as Creative Commons.

Takedown policy
Please contact us and provide details if you believe this document breaches copyrights.
We will remove access to the work immediately and investigate your claim.

This work is downloaded from Delft University of Technology.
For technical reasons the number of authors shown on this cover page is limited to a maximum of 10.

PROCEEDINGS OF SPIE

SPIEDigitalLibrary.org/conference-proceedings-of-spie

Coating layer on samples with roughness: numerical study for coherent Fourier scatterometry

D. Kolenov, S. Pereira

D. Kolenov, S. F. Pereira, "Coating layer on samples with roughness: numerical study for coherent Fourier scatterometry," Proc. SPIE 12619, Modeling Aspects in Optical Metrology IX, 126190V (10 August 2023); doi: 10.1117/12.2673768

SPIE.

Event: SPIE Optical Metrology, 2023, Munich, Germany

Downloaded From: https://www.spiedigitallibrary.org/conference-proceedings-of-spie on 16 Oct 2023 Terms of Use: https://www.spiedigitallibrary.org/terms-of-use

Coating layer on samples with roughness: numerical study for coherent Fourier scatterometry

D. Kolenov[a] and S. F. Pereira[a]

[a]Optics Research Group, Imaging Physics Department, Faculty of Applied Sciences, Delft University of Technology, Lorentzweg 1, 2628 CJ Delft, The Netherlands

ABSTRACT

For the development of integrated circuits, the accompanying metrology inside the fabrication process is essential. Non-imaging metrology of nanostructure has to be quick and non-destructive. The multilayers are crucial components of today's microprocessor nanostructures and reflective coatings. Coherent Fourier scatterometry (CFS), which is currently employed as a method for determining certain parameters of nanostructures and isolated particle detection, has not been investigated in the context of multilayer characterization. Retrieving the thickness of many wavelength-thick films using a coherent visible-range source at a full-complex-field measurement is the specific application where CFS might be advantageous. Furthermore, due to polishing in the realistic multilayers, the anticipated optical performance suffers from stochastic changes relating to surface roughness. Few non-imaging metrology methods take into consideration these statistic variances and thus are of interest for this study. Operating in the visible regime, CFS can become a viable candidate to provide cover layer reconstruction in the presence of surface roughness that has a correlation length bigger than the characteristic spot size i.e., in the range of microns. We present forward model results of multilayer structure as measured with visible range CFS modality. The influence of surface roughness is taken into account and the simulation results are discussed. Simulations of micron-sized layers of dielectric on silicon substrate suggest an influence on the far field intensity that motivates a future extended study on experimental multiple wavelength thick cover layer reconstruction in the presence of roughness.

Keywords: Optical metrology, multilayer, roughness, scatterometry

1. INTRODUCTION

With the advancement of coating technologies, such as thin films, nanostructures, and metamaterials, conventional measurement techniques such as standard ellipsometry[1] or surface profilometry[2] may be inadequate or impractical. Optical metrology techniques offer the capability to characterize these advanced coatings with high precision, providing valuable data for research, development, and innovation.[3] The modern techniques such as spectroscopic ellipsometry (SE), x-ray diffraction (XRD) and atomic force microscopy (AFM) have limitations themselves.[4,5]

Coherent Fourier scatterometry (CFS), studied in the paper, has shown to be a reliable tool for grating parameter reconstruction and for contamination/defect detection problem for flat substrates.[6,7] CFS possesses several strengths, including high localization precision, sensitivity, nondestructive nature, and the potential for multiplexing to enable high-throughput operation. However, this technique has not been extensively studied for thin film thickness reconstruction. In the initial approximation, it shares similarities with ellipsometry, exhibiting comparable strengths and weaknesses. Nevertheless, its unique characteristic of single-shot, many-angle measurements makes it potentially valuable for rapidly determining the thickness and material properties of multi-layer structures.

The objective of this contribution is not to challenge the current state-of-the-art, but rather to conduct a feasibility study on the application of CFS for thin-layer reconstruction. Additionally, incorporating roughness modeling, starting with simple interfaces like $SiO2$ or correlated stack such as $SiO2$ on Si, is crucial for comprehending the effects of roughness on light propagation, scattering, and ultimately, device functionality.

The remainder of the paper is organized as follows: Section 2 discusses the computational domain definition. It outlines the methodology used in the paper, including injecting pre-computed complex source spots, employing a computational domain geometry, generating roughness, and discussing expected behavior.

Modeling Aspects in Optical Metrology IX, edited by Bernd Bodermann, Karsten Frenner,
Proc. of SPIE Vol. 12619, 126190V · © 2023 SPIE · 0277-786X
doi: 10.1117/12.2673768

Downloaded From: https://www.spiedigitallibrary.org/conference-proceedings-of-spie on 16 Oct 2023
Terms of Use: https://www.spiedigitallibrary.org/terms-of-use

Section 3, in its first part discusses computational geometry influence on the far-field results in coherent Fourier scatterometry. It explains that truncating the near-field solution affects the accuracy of the far-field results, and the size of the computational domain can be adjusted based on the desired level of detail. The use of a far-field low-pass filter, positioning of extraction monitors and their impact on the intensity of reflected far-field results is also presented. In the second part it explores the impact of roughness on glass $SiO2$. This part analyzes the influence of roughness parameters, aliasing effects, and perturbed/scattered intensity at the air-glass interface, highlighting changes in intensity distribution based on different correlation lengths and roughness heights. The third part of this section studies the interference effects caused by reflections and refractions in a rough correlated stack of air-glass-silicon. It examines the parametric sweep of the thickness of the $SiO2$ layer and analyzes the normalized perturbed/scattered intensity, observing patterns of constructive and destructive interference and their impact on the intensity plot.

2. METHODS

An approach of the paper used to model coherent Fourier scatterometry for multi-layer cover-layer thickness retrieval in the presence of roughness interfaces involves injecting pre-computed complex valued source spots. The Richards and Wolf integral[8,9] is computed on the user-defined grid, the total extent of which is defined with src_x, src_y, generally for any z position in air medium, and further plugged in at the corresponding injection plane z_{inj} into Lumerical finite-difference time-domain (FDTD) solver. If mismatch between the discretization dx_{inj}, dy_{inj} of user-defined grid and of computational domain (CD or Ω) applies, the input field is interpolated on Ω. The (E_x, E_y, E_z) complex electric field components registered at every monitor/detector, z_{det1} and z_{det2} in Figure 1, are propagated to the far field according to built-in solver tools, described in referecences.[10–12] The computational domain Ω with dimensions $w_{x\Omega}, w_{y\Omega}, w_{z\Omega}$ and meshing discretization $dx_\Omega, dy_\Omega, dz_\Omega$ is surrounded with perfectly matched layer (PML) boundaries on all sides, thus modelling is non-periodic. Lastly, to capture subtle changes in the geometry of multi-layer, mesh can be increased locally with $dx_{OM}, dy_{OM}, dz_{OM}$. According to literature sources[13,14] the following behaviour of the model is expected:

+ Good method to model $2D$ rough surfaces that lead to diffuse light.
+ Extension to isolated imperfectness in non-periodic geometry.
+ Direct access to full complex field in a single simulation run.
− Possible artifacts due to the discontinuity at the edges of the simulation region.
− Large computational overhead.

Downloaded From: https://www.spiedigitallibrary.org/conference-proceedings-of-spie on 16 Oct 2023
Terms of Use: https://www.spiedigitallibrary.org/terms-of-use

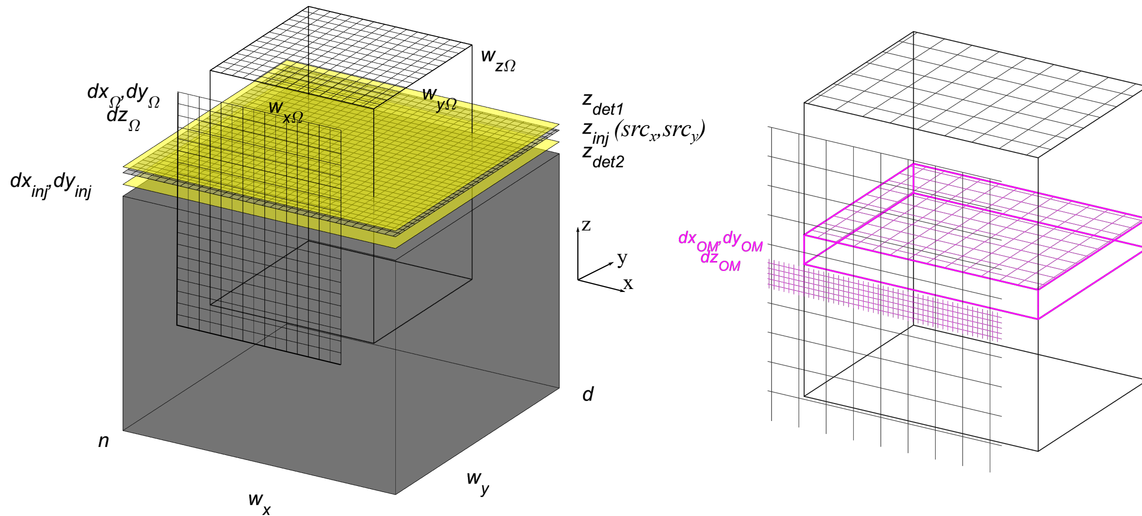

Figure 1. Sketch of the basic 3D model. The substrate dimensions in the transverse plane are controlled with w_x, w_y. Spot is pre-computed on external user-defined grid dx_{inj}, dy_{inj}, which has size src_x, src_y, and injected at z_{inj} above the top layer of material with refractive index of n and thickness d. Two monitors are installed to collect reflected, at z_{det1}, and total (reflected + incident), at z_{det2} field. The discretization of the computational domain Ω can be adjusted in three dimensions according to $dx_\Omega, dy_\Omega, dz_\Omega$. Any computation is truncated to the size of the Ω defined with $w_{x\Omega}, w_{y\Omega}, w_{z\Omega}$. Further the override mesh is essential for the roughness computations $dx_{OM}, dy_{OM}, dz_{OM}$.

N.B. The global coordinate system x, y, z is defined such way that top surface of the $SiO2$ substrate is located at $z = 0$, the position of every geometry or monitor element is centred about $(x, y) = (0, 0)$, thus expanding half-width in plus and minus directions laterally. When the cover layer is introduced it is grown in the $z \to +\infty$ direction. In the global coordinate system x, y, z the direction of propagation is backward, meaning from the injection plane, towards the $z \to -\infty$. The de-focused spot in air is evaluated such that it would attain the minimum size in the plane $z = 0$. Every simulation of the paper relies on the focused spot polarized along $x-$direction. Further, it is convenient to include the look-up table of the corresponding parameters used in the further studies of the paper with reference to the Figure number included (Table 1).

λ $[nm]$	Fig.	src_x,src_y $[\mu m]$	dx_{inj},dy_{inj} $[nm]$	w_x,w_y $[\mu m]$	$w_{x\Omega}$,$w_{y\Omega}$,$w_{z\Omega}$ $[\mu m]$	dx_Ω,dy_Ω, dz_Ω $[nm]$	dx_{OM}, dy_{OM}, dz_{OM} $[nm]$	z_{inj} $[nm]$	z_{det1} refl $[nm]$	z_{det2} tot $[nm]$
633	3	(15.825,15.825)	(14.8731,14.8731)	(16,16)	Sweep of $w_{x\Omega}$ $w_{y\Omega}$ [1:1:15] fixed $w_{z\Omega}$ 0.2	(100,100,10)	disabled	100	N/A	50
633	4	(15.825,15.825)	(14.8731,14.8731)	(16,16)	Sweep of $w_{x\Omega}$ $w_{y\Omega}$ [1:1:15] fixed $w_{z\Omega}$ 0.2	(100,100,10)	disabled	100	125	N/A
633	5	(15.825,15.825)	(14.8731,14.8731)	(16,16)	(3,3,0.2)	(100,100,10)	disabled	100	N/A	50 sweep of fc
405	6	(6.075,6.075)	(12.15,12.15)	(10,10)	(3,3,1.7)	(20,20,10)	(10,10,10) complete Si substrate	sweep of [1500:-25:100]	1525 z_{inj} + 25 N/A	N/A N/A z_{inj}-25
633	7	(15.825,15.825)	(14.8731,14.8731)	(10,10)	(3,3,0.2)	(100,100,10)	(90,90,1) centered at interface (5000,5000,32) span	100	125	N/A
633	8	(15.825,15.825)	(14.8731,14.8731)	(10,10)	(3,3,0.2)	(100,100,10)	dz_{OM} is fixed to 1 sweep of [100:-10:10] centered at interface	100	125	N/A
633	9 and 10	(15.825,15.825)	(14.8731,14.8731)	(10,10)	(3,3,0.2)	(100,100,10)	(90,90,1) centered at interface (5000,5000,32) span	100	125	50
405 633	11	(6.075,6.075) (9.495,9.495)	(12.15,12.15) (18.99,18.99)	(3.2,3.2)	(3,3,1.7)	(20,20,10)	(20,20,1) same mesh centered at each interface (3200,3200,21)	-1500	1525	N/A

Table 1. The summary of the geometry and meshing parameters for the models estimated in the paper.

Downloaded From: https://www.spiedigitallibrary.org/conference-proceedings-of-spie on 16 Oct 2023
Terms of Use: https://www.spiedigitallibrary.org/terms-of-use

It is evident that the w_x, w_y computational domain size is consistently smaller than the defined geometry or the spot size. For every simulation case of the paper, the size of the glass slab was used is $w_z = 1\mu$m. In cases where it is not essential, such as the air-glass interface, only a small portion ($w_{z\Omega} = 0.2\mu m$) of the geometry is utilized in the computational domain. However, when conducting a parametric sweep for layer thickness, as seen in the air-glass-silicon interface, the computational domain is determined by the expanded geometry and $w_{z\Omega}$ is set to $1.7\mu m$.

The corresponding constants used in the paper are from the Palik[15] database entry of Lumerical (Table 2).

	SiO2	Si
$\lambda = 405nm$	1.46958+1j*1.11e-16	5.4254+1j*0.330936
$\lambda = 633nm$	1.45702	3.88126+1j*0.018938

Table 2. The summary of refractive index values used in the modelling of the paper.

The rough surface is described by its root mean square amplitude h_{RMS} and correlation length L_c. If for particular surface realization the horizontal lag is introduced $\vec{\delta}$ the auto correlation function $\frac{h(\vec{r})h(\vec{r}+\vec{\delta})}{h_{RMS}}$ of surface heights $h(\vec{r})$ can be evaluated. Further, the average is carried out over all positions on the surface $\frac{<h(\vec{r})h(\vec{r}+\vec{\delta})>}{h_{RMS}}$ and assuming that the surface correlation function is Gaussian, the correlation length can be achieved such that it satisfies $\frac{<h(\vec{r})h(\vec{r}+\vec{\delta})>}{h_{RMS}} = \exp\Big(-\big(\frac{\vec{\delta}}{L_c}\big)^2\Big)$. In practice to generate the roughness, a random matrix of values is created in k-space. Since the random values generation is a stochastic process by using a fixed seed value, the random number generator of the model is initialized consistently for each run. This ensures reproducibility of the model runs. The generated matrix is then subjected to a Gaussian filter, followed by a Fourier transform to convert it back to the real space. More information on this process can be found in reference,[13] which is the article that introduces the built-in surface synthesizer of Lumerical that is used in this study.

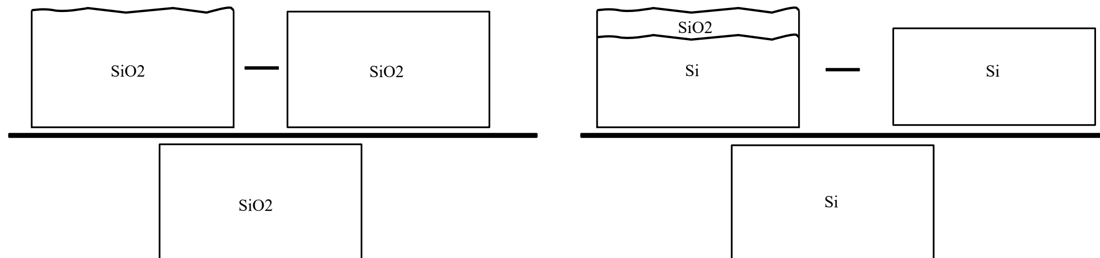

Figure 2. Sketch explaining the normalization process for the perturbed far-field solution.

Finally, in Sections 3.2 and 3.3, normalization is employed to explain the impact of surface roughness on the simulated intensity. The left figure in the sketch above (Figure 2) illustrates the rationale behind the normalization in Section 3.2, while the right figure demonstrates the normalization discussed in Section 3.3. The difference between the corresponding intensities of the rough and non-rough (reference) geometries indicates the presence of a scattered or perturbed field. This difference can still be calculated using either the reflected z_{det1} or the total z_{det2} detector/monitor. The division of a scattered intensity by intensity that corresponds to non-rough geometry is needed to observe a fractional change in magnitude. In the right sub-figure, one can observe the concept of a correlated stack, where all interfaces possess identical roughness functions.

3. RESULTS

3.1 Domain definition

The truncation of the near-field solution has a direct effect on the far-field results. In principle the infinite monitor plane upon reflection would most accurately represent the underlying interaction, however that is not a feasible scenario due to computational overhead. The high-frequency components of electric field oscillations

Downloaded From: https://www.spiedigitallibrary.org/conference-proceedings-of-spie on 16 Oct 2023
Terms of Use: https://www.spiedigitallibrary.org/terms-of-use

that arise from the reflection of the focused beam spot from the underlying structure are gradually eliminated to improve computational efficiency. In the case of simple air to glass interface without roughness the total field is giving correct qualitative representation of the focused spot reflection from the flat surface.

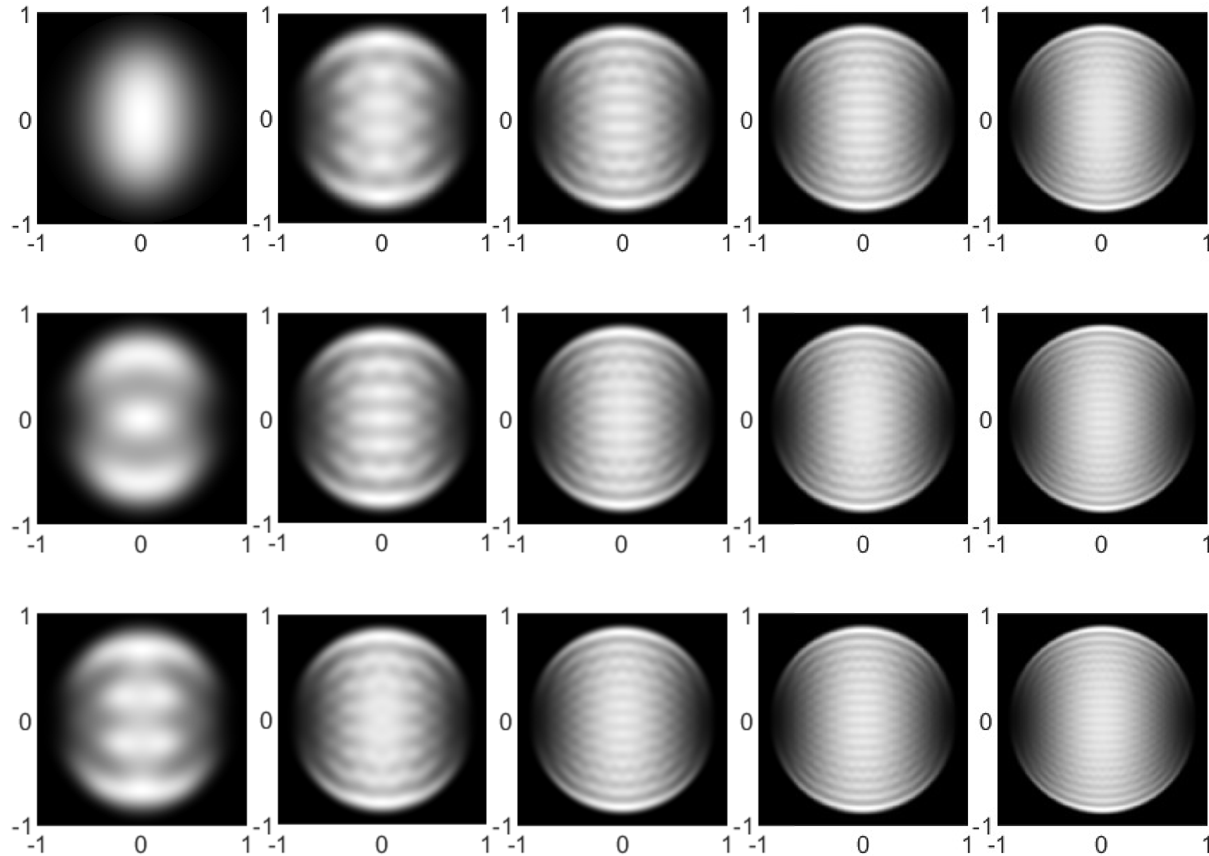

Figure 3. The effect of Ω truncation on far-field intensity at total monitor in the square transverse plane described by $w_{x\Omega} = w_{y\Omega} = [1 : 1 : 15]\mu m$. The transverse domain size is increased top to bottom and from left to right starting from $1 \times 1\mu m$ to $15 \times 15\mu m$ in steps of $1\mu m$.

The presence of a reflection minimum in the x-direction of the pupil at the corresponding Brewster angle of p-polarized light serves as an indication of correctness. The numerical aperture (NA) discussed in the paper is consistently 0.9, and the intensity distribution is evaluated on the k_x, k_y grid. The complete pupil, representing propagating waves in air, is normalized to the range from -1 to +1. Figure 3 demonstrates that the simulation of the far field yields the highest level of detail in the lower right corner when using a domain size of $15 \times 15\mu m$ (extraction monitor is scaled accordingly). However, it is not necessary to employ such a large simulation domain, as the most crucial features of the field are already revealed starting from a domain size of $3 \times 3\mu m$.

To ensure a comprehensive analysis, we present Figure 4 to showcase the influence of Ω truncation on the intensity of the reflected far-field results. When the incident field is not registered at the monitor, one can observe that the intensity distribution is not qualitatively accurate. Specifically, the Brewster angle is located in the incorrect part of the pupil.

Downloaded From: https://www.spiedigitallibrary.org/conference-proceedings-of-spie on 16 Oct 2023
Terms of Use: https://www.spiedigitallibrary.org/terms-of-use

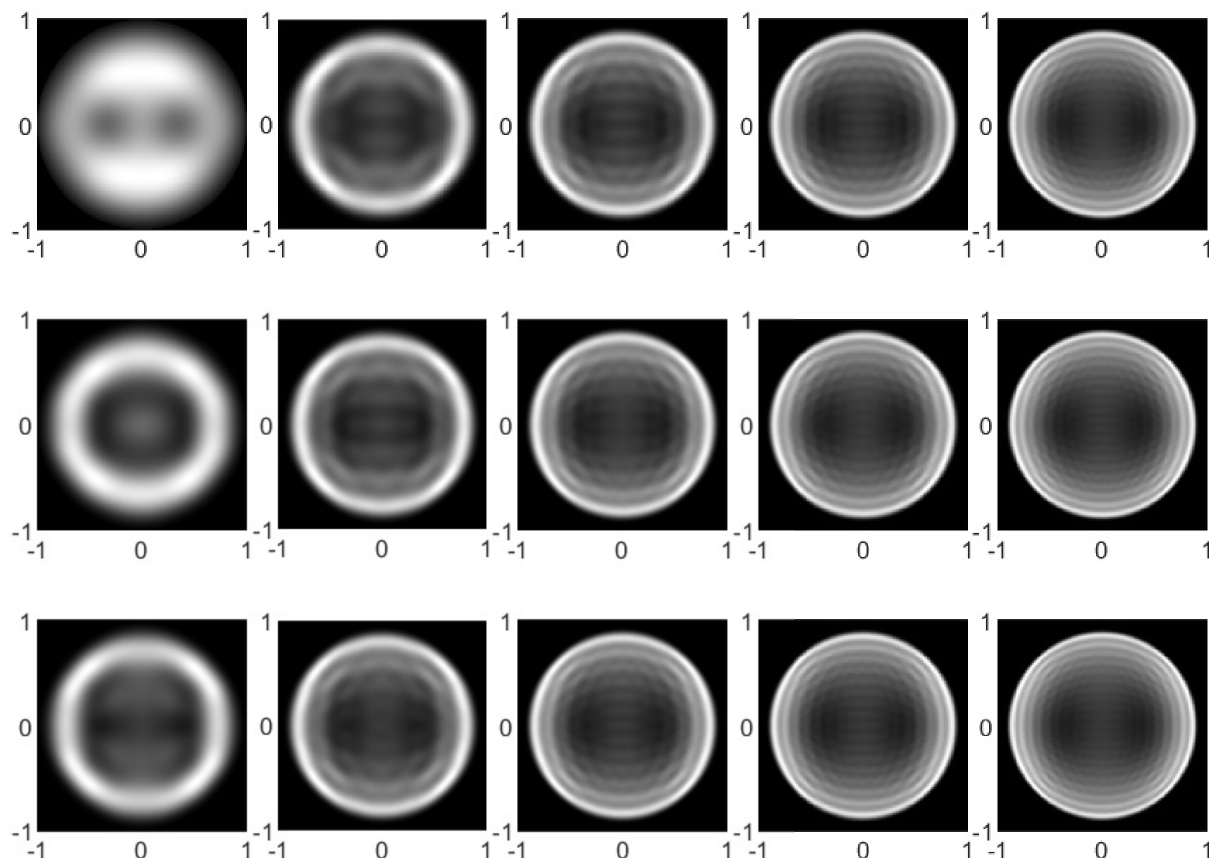

Figure 4. The effect of Ω truncation on far-field intensity at reflected monitor in the square transverse plane described by $w_{x\Omega} = w_{y\Omega} = [1:1:15]\mu m$. The transverse domain size is increased top to bottom and from left to right starting from 1×1 mum to 15×15 mum in steps of $1\mu m$.

In this paper, we utilize the reference reflected field, which corresponds to a flat interface, to subsequently quantify the impact of the introduced roughness. Although it is evident that the intensity distribution registered at this plane is unsuitable for reconstruction, we include this reflected intensity for the sake of completeness, allowing us to evaluate the effect of substrate roughness both before and after its introduction.

In the context of experimental reconstruction relying on the correlation between measured and simulated far-field results, it is conceivable that fluctuations in the simulated field may arise. To enhance the reconstruction process, the utilization of a far-field low-pass filter can be considered. The filter introduced internally in Lumerical software and is controlled with a single parameter f_c, ranging from 0 to 1 and effect of no filtering $f_c = 0.1$ to $f_c = 0.9$ (filtering almost up to the edge of the monitor) is summarized in Figure 5.

Downloaded From: https://www.spiedigitallibrary.org/conference-proceedings-of-spie on 16 Oct 2023
Terms of Use: https://www.spiedigitallibrary.org/terms-of-use

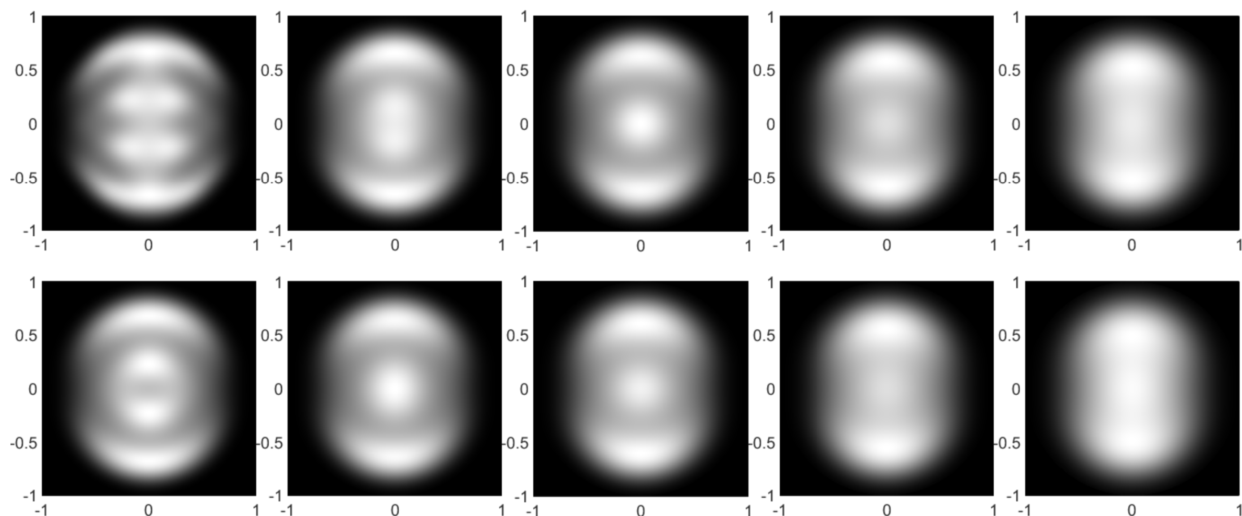

Figure 5. The effect of f_c corner frequency $f_c = [0 : 0.1 : 0.9]$ low-pass far-field filter on the total far-field intensity for the fixed $w_{x\Omega} = w_{y\Omega} = 3 \times 3 \mu m$. Higher f_c going from top to bottom and from left to right.

N.B. The far-field filter does not improve the accuracy of the projection, to enhance accuracy, it is necessary to widen the monitor and simulation region to capture a greater portion of the fields that will propagate to the far field.[16] If applied to periodic structures that exhibit an infinitely extending repetitive pattern, the use of filtering to eliminate high-frequency components can disrupt the inherent periodicity and introduce inaccuracies in the simulation results. Therefore, it is recommended to avoid applying the far-field filter in such cases. In the paper we haven't used the filter to generate the results of Section 3.2 and 3.3.

For the far-field intensity reconstruction of multi-layer structures, it is necessary to generate parametric sweeps of different layer thicknesses. In such cases, the size of the computational domain can be set in relation to the maximum thickness of the structure $w_{z\Omega} = 1.7 \mu m$, while the transverse domain size can be reasonably fixed to minimize computational overhead $w_{x\Omega} = w_{y\Omega} = 3 \mu m$. However, the choice of the extraction monitor plane remains crucial as it directly impacts the simulation outcome.

In Figure 6, the 2D correlation coefficient r is calculated for the simulated far-field intensity distributions. The reference value $r = 1$ is chosen for the position of the source injection at $z_{inj} = 1500$ nm. In all three cases, a sweep is conducted to select the injection plane progressively closer to the surface of Si, with positions ranging from 1500 nm to 100 nm in increments of -25 nm. The exhibited behavior (different realizations of intensity) renders it impractical to depend on the distribution of the simulated far-field, considering the essential need for qualitative properties in the reconstruction process.

Downloaded From: https://www.spiedigitallibrary.org/conference-proceedings-of-spie on 16 Oct 2023
Terms of Use: https://www.spiedigitallibrary.org/terms-of-use

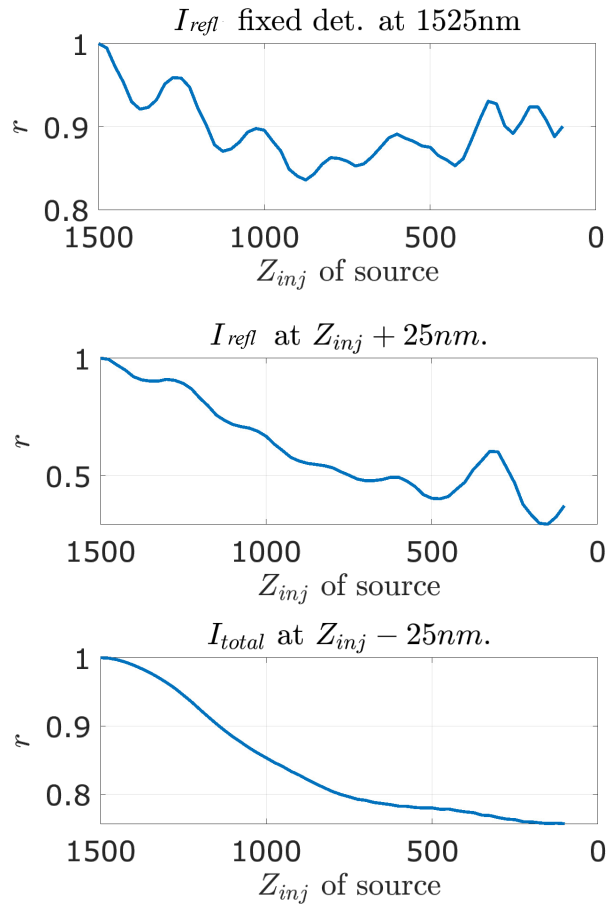

Figure 6. The effect of injection and monitor plane position selection for focusing in air and reflection from Si substrate, $\lambda = 405nm$ and $NA = 0.9$.

The top figure in Figure 6 shows a fixed reflected monitor configuration. The middle figure illustrates a moving reflected monitor (linked by a constant offset from source $z_{inj} + 25$ nm). Lastly, the bottom figure shows a moving total monitor (linked by a constant offset from source $z_{inj} - 25$ nm). The Figure 6 gives clear indication that the simulated intensity distribution would change down to $r = 0.5$ if, for instance, reflected field monitor is moved together behind the varied z_{inj}.

3.2 Rough glass interface

As $SiO2$ is commonly used as a substrate in many optical and electronic devices its surface roughness can have a significant impact on the performance of these devices. The impact of roughness perturbation can be summarized by calculating the difference between the intensity field of a rough structure and that of a flat structure $I_{pert} = I_{rough} - I_{flat}$. When considering a simple air-glass interface, the presence of surface roughness leads to diffuse scattering, causing light to effectively travel outside the extraction monitor or collection optics. Therefore, it is reasonable to expect that I_{pert} can take negative values.

Downloaded From: https://www.spiedigitallibrary.org/conference-proceedings-of-spie on 16 Oct 2023
Terms of Use: https://www.spiedigitallibrary.org/terms-of-use

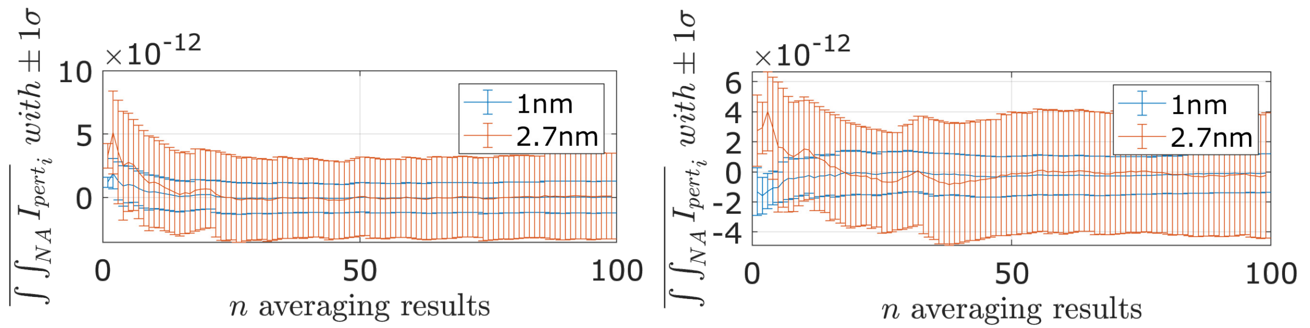

Figure 7. Integrated I_{pert} at the reflected monitor for $SiO2$ rough surface of either 1 or 2.7nm h_{RMS} as the function of random seed. The $L_{cx} = L_{cy} = 1.1\mu m$ and in the left figure random seed is generated sequentially and in the right figure random seed is generated randomly. The $\lambda = 633nm$ and $NA = 0.9$. The $dx_{OM} = dy_{OM} = 90$nm.

Figure 7 shows the mean $\overline{X}$ and sample standard deviation σ_x of n realizations of random roughness seeds. The mean is $\overline{X} = \overline{\iint_{NA} I_{pert_i}}$, where i ranges from 2 to $n = 100$, and integration over the pupil is effectively adding all the points that fit inside the circle of $NA = 0.9$. These random seeds realizations effectively govern the spatial distribution of surface heights and, as anticipated, the surface roughness exhibits an increase with the rise in h_{RMS}. There is no clear influence of having either sequential or randomly selected seed number. However, the noteworthy observation is that with an increasing number of realizations, there is minimal disparity in the mean intensity values, while the standard deviation becomes larger.

There is known aliasing effect in signals theory[17] which is also crucial for surface roughness studies.[18] For our simulation problem when relatively lower, sub-wavelength, correlation lengths needs to be simulated, the region that encloses rough surface profile has to be meshed higher than the rest of the domain and that is controlled with override mesh $dx_{OM}, dy_{OM}, dz_{OM}$.

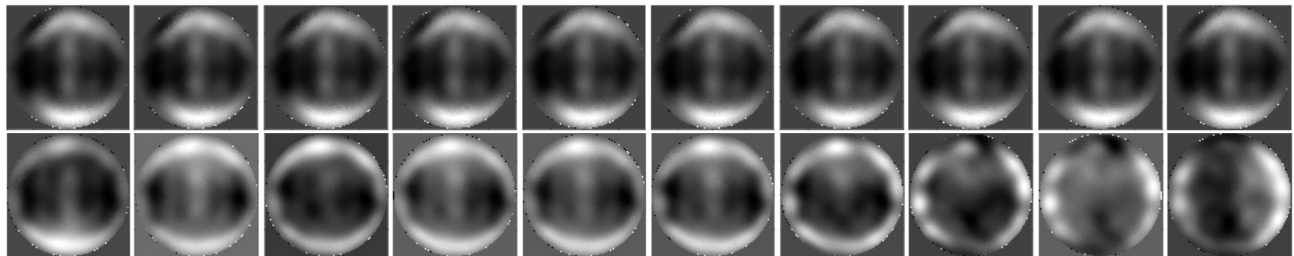

Figure 8. The perturbed intensity, I_{pert}, at the reflected monitor for a rough surface of $SiO2$ is plotted as a function of the override mesh parameter, $dx_{OM} = dy_{OM}$, which varies in the range of $100 : -10 : 10$ nm. The upper row corresponds to $L_{cx} = L_{cy} = 1.1\mu m$, while the bottom row corresponds to $L_{cx} = L_{cy} = 40$ nm.

The effect of aliasing is demonstrated in Figure 8. The override mesh discretization, denoted by dx_{OM} and dy_{OM}, is progressively decreased from 100 nm to 10 nm in increments of 10 nm. In the upper row of Figure 8, which corresponds to a correlation length of $L_{cx} = L_{cy} = 1.1\mu m$, no noticeable change in the perturbation intensity I_{pert} is observed. However, for the surface with a relatively small, sub-wavelength correlation length of $L_{cx} = L_{cy} = 40$ nm, significant changes in the intensity distribution can be seen.

In Figure 9 we demonstrate the perturbations that occur at the reflected and total plane for the simple air to glass interface with roughness. One can observe that due to the fixed random seed the far-field intensities keep very similar distribution within same row of the bottom panel of Figure 9. Further changes in correlation length are also traceable in the far field such as in upper and lower row of "Scattered at reflected" and "Scattered at total" panels. The roughness height is increased in the vector of $1, 2.7, 10$ nm, which is also evident in the

Downloaded From: https://www.spiedigitallibrary.org/conference-proceedings-of-spie on 16 Oct 2023
Terms of Use: https://www.spiedigitallibrary.org/terms-of-use

corresponding columns from left to right. This increase is visible as an amplitude growth of the perturbed intensity.

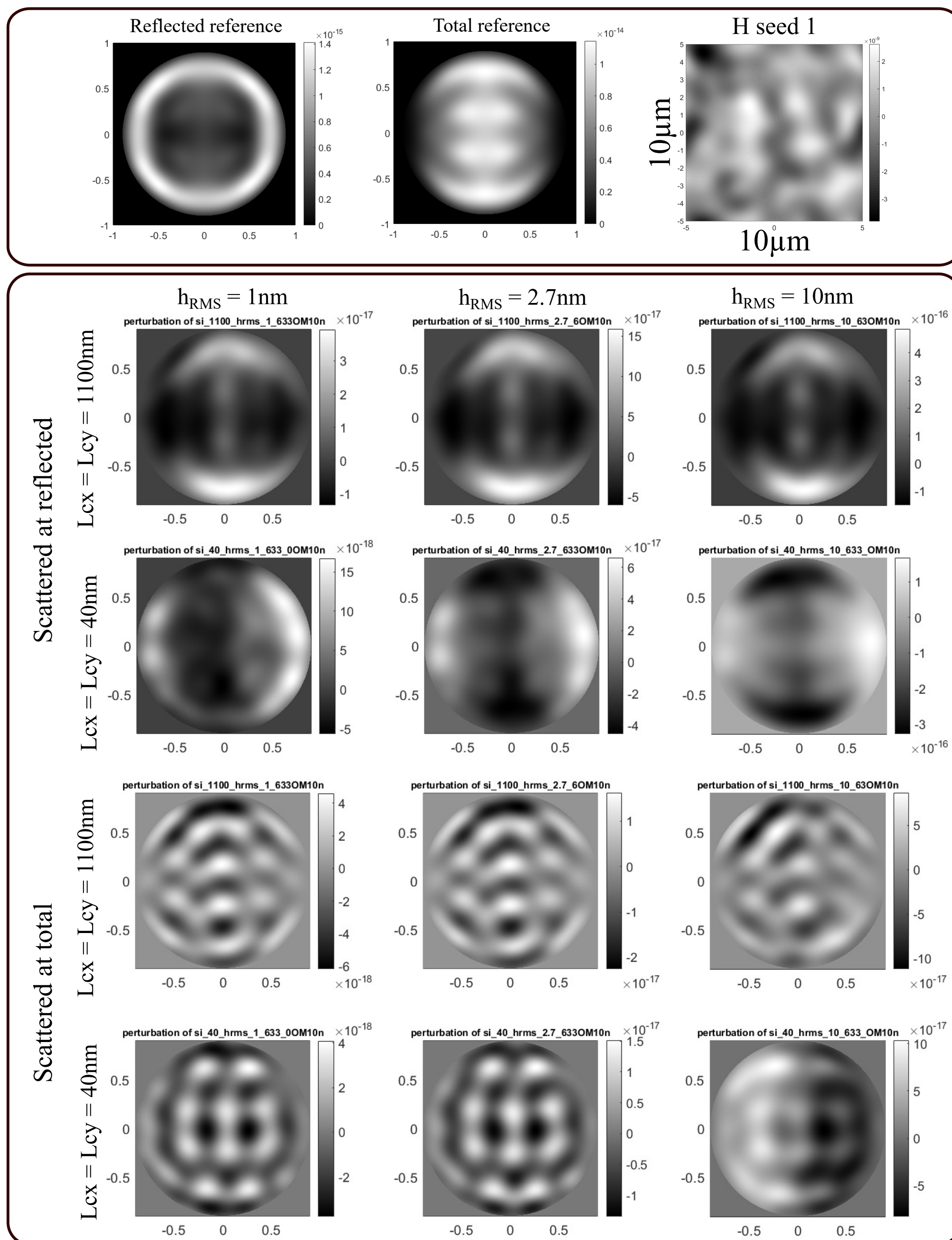

Figure 9. In the upper panel, from left to right, we show the reference reflected intensity, total intensity, and $SiO2$ surface roughness realization for $L_{cx} = L_{cy} = 1.1\mu m$ and $h_{RMS} = 1$ nm. In the bottom panel far field intensity patterns for I_{pert} are shown. Two upper rows represent reflected monitor and the two lower rows represent total monitor. Two correlation lengths $1.1\mu m$ and 40nm are considered and the h_{RMS} takes three values $1, 2.7, 10$nm. The $\lambda = 633nm$ and $NA = 0.9$. The $dx_{OM} = dy_{OM} = 10$nm.

Downloaded From: https://www.spiedigitallibrary.org/conference-proceedings-of-spie on 16 Oct 2023
Terms of Use: https://www.spiedigitallibrary.org/terms-of-use

To summarize the effect of top surface roughness for $SiO2$ the perturbation normalized intensity is calculated as $I_{pert\,norm} = (\iint_{NA} I_{pert})/(\iint_{NA} I_{flat})$. The mean and standard deviation of $n = 5$ realizations of random roughness seeds are shown for $\overline{I_{pert\,norm_i}}$, where i ranges from 1 to n. The y-axis of the figures in Figure 10 effectively represents the absolute percentage change in perturbed/scattered normalized intensity generated based on the reflected (left) or total (right) monitor. The upper panel represents 1.1μm and bottom panel represents 40nm correlation length.

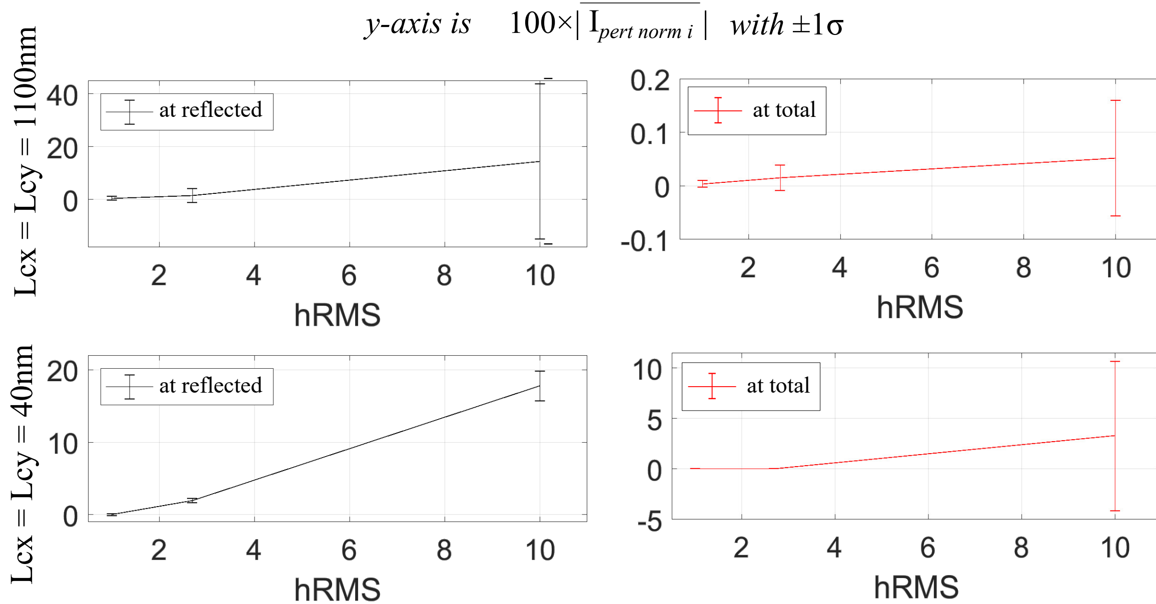

Figure 10. The absolute percentage change in perturbed/scattered normalized intensity generated based on the reflected (left) or total (right) monitor as a function of the rough surface of $SiO2$, where h_{RMS} takes on three values: 1 nm, 2.7 nm, and 10 nm. The $L_{cx} = L_{cy} = 1.1\mu m$ in top panel and $L_{cx} = L_{cy} = 40$nm in the bottom panel. The $\lambda = 633nm$ and $NA = 0.9$. The $dx_{OM} = dy_{OM} = 10$nm.

The overall trend observed in the sub-figures above is that there is a larger change in simulated intensity with higher h_{RMS}, particularly in the case of reflected monitor compared to total monitor intensity. For example, in the bottom panel, there is an average change of approximately $\approx 18\%$ for $L_{cx} = L_{cy} = 40$ nm in the reflected monitor, whereas the change is around $\approx 3\%$ in the total monitor. The model demonstrates sensitivity to changes in correlation length as well. When the same h_{RMS} is considered with a shorter correlation length, surface becomes more rough and accordingly the intensity distribution shows more perturbation. This behavior regarding the correlation length was also emphasized in the reference.[19]

3.3 Rough correlated stack air-glass-silicon

Interference from reflections and refractions at the interfaces of a dielectric layer affects the light measured at the detector, causing variations in intensity and phase. This interference complicates the precise determination of the layer's thickness and optical properties. Accurate retrieval of the layer's properties requires careful analysis and interpretation of the complex interference patterns generated in simulations. Moving on to Figure 11, we present the parametric sweep of the thickness of the correlated stack rough $SiO2$ as the cover layer on Si, as a function of two wavelengths: $\lambda = 405$ and $\lambda = 633$nm. The $SiO2$ thickness is varied as $d = [10 : 10 : 1000]$nm and perturbed intensity (at reflected monitor) is normalized to the solution of the flat Si such that $I'_{pert\,norm} = (\iint_{NA} I'_{pert})/(\iint_{NA} I_{flat\,nolayer})$. In this sub-section the metric to describe the roughness is slightly different from the previous sub-section because $I'_{pert} = I_{rough} - I_{flat\,nolayer}$. The solid blue curves in the graph represent the average of five random seeds of $SiO2$ correlated stack roughness, with $h_{RMS} = 1$ nm and $L_{cx} = L_{cy} = 1.1\mu m$. The error bars indicate the range of $\pm 1\sigma$ deviation due to the introduced roughness.

Downloaded From: https://www.spiedigitallibrary.org/conference-proceedings-of-spie on 16 Oct 2023
Terms of Use: https://www.spiedigitallibrary.org/terms-of-use

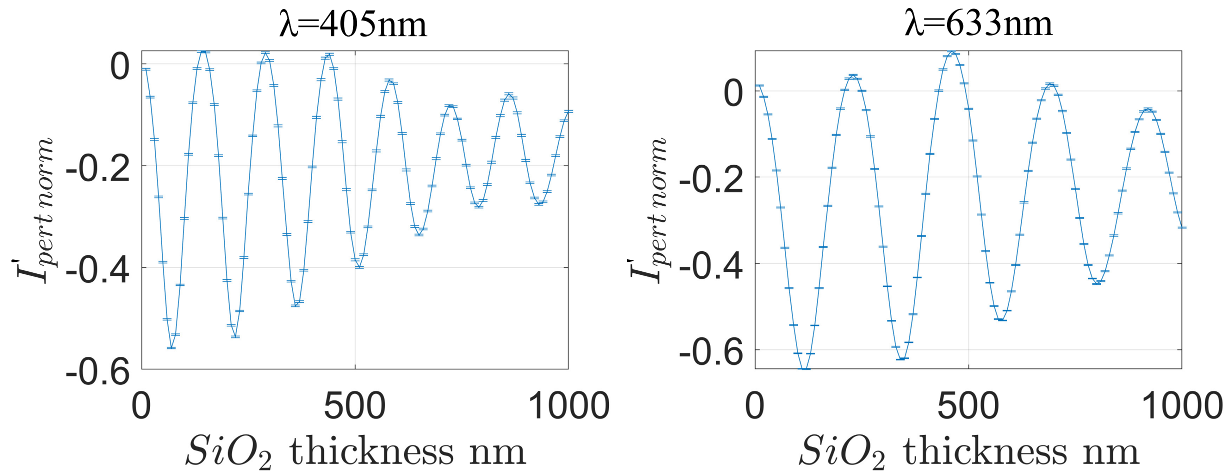

Figure 11. The integrated perturbed intensity as the function of $SiO2$ cover layer thickness on Si normalized to uncovered solution with bare Si. The case of $\lambda = 405$nm is on the left and $\lambda = 633$nm is on the right. The solid line type represents an average of five random seeds of $SiO2$ correlated stack roughness with $h_{RMS} = 1$nm and $L_{cx} = L_{cy} = 1.1\mu m$, the error bars represent $\pm 1\sigma$.

In Figure 11, what we observe are the negative values of $I'_{pert\,norm}$. The reason behind this is the decrease in intensity of the reflected field due to glass and silicon structure in comparison to the flat only silicon counterpart. The shapes of the curves in both cases is dictated by constructive and destructive interference, creating a series of peaks and valleys in the intensity plot. This pattern of positions of minima for $\lambda = 405$nm occurs at $[70, 220, 360, 510, 650, 790, 930]$nm and for the plane wave normal incidence case analytically should give $[68.8972, 206.6917, 344.4862, 482.2807, 620.0751, 757.8696, 895.6641]$nm and $\lambda = 633$nm occurs at $[120, 340, 580, 800]$nm and analytically $[108.6121, 325.8363, 543.0605, 760.2847]$nm. The analytical formula used here is valid for $n_3 > n_2 > n_1$ scenario (silicon, glass and air in our case) $t_{AR} = (m + 1/2) * (\lambda/(2 * n_2))$ for $m = 0, 1, 2, \ldots$. The reduction of the amplitude of the signal towards thicker layer of the $SiO2$ in both cases shall not be confused with the effect of absorption because glass is dielectric. The domain geometry and truncation of the near field solution must be the key factors here.

4. CONCLUSIONS

In conclusion, this study emphasizes the significant impact of surface roughness on both single-layer $SiO2$ and two-layer $SiO2/Si$ substrates. When modeling with the intention of experimental reconstruction based on forward model results or simulated data, careful consideration must be given to the selection of model parameters and the modeling approach itself. The simulated far-field distribution with pre-computed focused spot injection can only be reliably applied when it can be compared against a reference ground truth, such as analytical solutions or results from other simulation tools. In such cases, the injection plane and monitor positions are fixed, allowing for changes solely in the object geometry.

Further investigation reveals that surface roughness noticeably affects the intensity of the perturbed/scattered field. This effect is more pronounced in the intensity of reflected monitor compared to the total monitor detector, highlighting the importance of selecting appropriate extraction monitors for 3D modeling of roughness with source injection. The correlation length of the surface roughness emerges as a significant factor influencing the extent of perturbation in the intensity distribution. Simulations demonstrate that higher root mean square (RMS) roughness values lead to more substantial changes in intensity, particularly if registered at reflected monitor. As expected, the correlation length influences both the roughness height and the resulting intensity distribution.

In the context of a rough correlated stack consisting of air-glass-silicon, the interference effects resulting from reflections and refractions at the interfaces play a crucial role. These interference effects introduce variations in intensity, although the effect is minor for the demonstrated example of 1nm $hRMS$. In the real experimental

Downloaded From: https://www.spiedigitallibrary.org/conference-proceedings-of-spie on 16 Oct 2023
Terms of Use: https://www.spiedigitallibrary.org/terms-of-use

setup of coherent Fourier scatterometry (CFS) it can be inferred that layers with a low correlation length (frequent variations in a transverse plane) will introduce uncertainty during the reconstruction process.

ACKNOWLEDGMENTS

This project receives funding from EMPIR JRP 20IND04 "ATMOC".

REFERENCES

[1] Azzam, R. M., Bashara, N. M., and Ballard, S. S., "Ellipsometry and polarized light," *Physics Today* **31**(11), 72 (1978).

[2] Yoshizawa, T., [*Handbook of optical metrology: Principles and Applications*], CRC press (2017).

[3] Fujiwara, H., [*Spectroscopic ellipsometry: principles and applications*], John Wiley & Sons (2007).

[4] Mahmood, A., Nasar, A., Mircea, C., Bensaada Laidani, N., De Hosson, J., et al., "Handbook of modern coating technologies: Advanced characterization methods," in [*Handbook of Modern Coating Technologies: Advanced Characterization methods*], **2** (2021).

[5] West, P. E., "Introduction to atomic force microscopy theory, practice, applications," (2007).

[6] Kumar, N., El Gawhary, O., Roy, S., Pereira, S., and Urbach, H., "Phase information in coherent fourier scatterometry," in [*Optical Measurement Systems for Industrial Inspection VIII*], **8788**, 481–488, SPIE (2013).

[7] Yin, H., Kolenov, D., and Pereira, S. F., "Coherent fourier scatterometry nanoparticle detection enhanced by synthetic optical holography," *Optics Letters* **47**(15), 3840–3843 (2022).

[8] Richards, B. and Wolf, E., "Electromagnetic diffraction in optical systems, ii. structure of the image field in an aplanatic system," *Proceedings of the Royal Society of London. Series A. Mathematical and Physical Sciences* **253**(1274), 358–379 (1959).

[9] Costa Assafrao, A., *On super resolved spots in the near-field regime*, PhD dissertation, TU Delft (2013).

[10] Lumerical, "Far field projections in fdtd overview," (2016).

[11] Lumerical, "Far field projections from a box of monitors," (2016).

[12] Taflove, A., Hagness, S. C., and Piket-May, M., "Computational electromagnetics: the finite-difference time-domain method," *The Electrical Engineering Handbook* **3**, 629–670 (2005).

[13] Lumerical, "Bidirectional scattering distribution function (bsdf)," (2016).

[14] Maradudin, A. A., [*Light scattering and nanoscale surface roughness*], Springer Science & Business Media (2010).

[15] Palik, E. D., [*Handbook of optical constants of solids*], vol. 3, Academic press (1998).

[16] Lumerical, "Using spatial filtering to avoid truncating fields in far field projections," (2016).

[17] McClellan, J. H., Schafer, R. W., and Yoder, M. A., [*Dsp first*], Pearson Education (2017).

[18] Mack, C. A., "Systematic errors in the measurement of power spectral density," *Journal of Micro/Nanolithography, MEMS, and MOEMS* **12**(3), 033016–033016 (2013).

[19] Jiang, R., Chen, K.-S., Li, Z.-L., Du, G.-Y., and Tian, W.-J., "Entropy measure of generating random rough surface for numerical simulation of wave scattering," *IEEE Transactions on Geoscience and Remote Sensing* **59**(5), 3623–3641 (2020).

Downloaded From: https://www.spiedigitallibrary.org/conference-proceedings-of-spie on 16 Oct 2023
Terms of Use: https://www.spiedigitallibrary.org/terms-of-use